Acta Materialia 289 (2025) 120863

Contents lists available at ScienceDirect

Acta Materialia

journal homepage: www.elsevier.com/locate/actamat

Full length article

Scalar permeability microstructure model considering crystallographic texture and grain size for magnetic evaluation of anisotropy in steel

Jun Liu [a,*], Claire Davis [b], Shuaichao Yue [c], Mohsen Aghadavoudi Jolfaei [b], Jialong Shen [d], Yongjian Li [c]

[a] School of Engineering, Cardiff University, Queens Building, 14-17 The Parade, Cardiff, CF24 3AA, United Kingdom
[b] Advanced Steel Research Centre, Warwick Manufacturing Group, University of Warwick, Coventry CV4 7AL, United Kingdom
[c] State Key Laboratory of Reliability and Intelligence of Electrical Equipment, Hebei University of Technology, Tianjin, 300130, China
[d] Key Laboratory of New Processing Technology for Nonferrous Metal & Materials, Ministry of Education/Guangxi, Guilin University of Technology, Guilin 541004, China

ARTICLE INFO

Keywords:
Texture
Finite element analysis
Microstructure
Magnetic anisotropy
Grain size

ABSTRACT

This paper presents a finite element microstructure model specifically designed to predict scalar anisotropic magnetic permeability. The model integrates crystallographic texture and grain size considerations within specific microstructures, offering a significant advancement in the analysis of scalar permeability and magnetic anisotropy. The model's precision and robustness have been validated with two types of steel: commercial-grade grain-oriented electrical steel and industrially recrystallised Interstitial-Free steel. Validation was accomplished through comparative magnetic measurements using a modified rotational single sheet tester under varying magnetic field strengths. Additionally, the model employs a generalised power law approach to account for grain size effects, adapting different power laws as necessary. This aspect of the model has been corroborated with experimental data from the literature.

1. Introduction

Anisotropy in steel, the directional dependency of material properties, can be either beneficial or detrimental. Certain steels, like grain-oriented electrical steels (GOES) and deep drawing grades, are engineered to exploit these directional properties for optimal performance in specific applications. Conversely, undesirable anisotropy, as seen in non-oriented electrical steels and hot-rolled plates, can compromise the quality of these products. In either case, it is imperative to be able to non-destructively and accurately evaluate the anisotropy in steels. Magnetic Non-Destructive Evaluation (NDE) techniques are emerging as a prominent tool, offering significant value beyond traditional methods for microstructural analysis and property assessment in steel. Due to their inherent directional measurement capabilities, most magnetic NDE systems are intrinsically sensitive to magnetic anisotropy, providing an effective means of assessment [1].

Iron and steel crystal structures exhibit magnetic anisotropy, primarily due to the alignment of magnetic dipoles within their crystal cells [2]. This inherent magnetic anisotropy in each grain influences the overall behaviour of polycrystalline steels. When grains are randomly oriented, the steel tends to behave isotropically. However, the presence of preferred crystallographic orientations, or crystallographic texture, imparts a noticeable anisotropy to the material's average properties.

This understanding has led to models that predict anisotropic properties of polycrystalline materials by averaging the properties of single crystals. Daniel et al. [3] estimated the effective magnetic permeability of polycrystalline materials based on single-crystal anisotropy and effective medium approximations. L. Kestens [4] took a more basic and simplified approach proposing an 'A' parameter, as opposed to a fundamental magnetic property, that averages the minimum angle between the magnetisation (implicitly assumed to be homogeneous) and the closest easy magnetic direction to characterise the so-called magnetic quality of a given texture for non-oriented electrical steels.

Both Daniel's and Kestens' models overlooked significant aspects of the microstructure, particularly the morphology of individual grains and the overall microstructure, which can influence magnetic flux behaviours and, consequently, the effective permeability. These models are effective for uniform, equiaxed single-phase materials but cannot be applied to more complex microstructures. For instance, alignment in the microstructure, especially of the second phase, often occurs during steel processing, such as rolling [5], and is sometimes present in the final product. Examples include superduplex stainless steel (banded

* Corresponding author.
E-mail addresses: liuj118@cardiff.ac.uk (J. Liu), Claire.Davis@warwick.ac.uk (C. Davis).

https://doi.org/10.1016/j.actamat.2025.120863
Received 25 August 2024; Received in revised form 15 January 2025; Accepted 22 February 2025
Available online 7 March 2025

austenite and ferrite structures), dual-phase steels (banded ferrite and martensite), or hot-rolled C-Mn grades (banded ferrite and pearlite structures), which can lead to magnetic anisotropy. Zhou et al. [6] predicted the effective permeability for dual-phase steel microstructures using digitised and processed real micrographs (identifying different phases) through finite element (FE) modelling. Whilst this approach allows for the study of the separate effects of aligned microstructures, phase balance, and grain size [7], it does not account for the effect of crystallographic texture. Ignoring this factor could result in misleading predictions and interpretations if textures significantly influence magnetic properties and anisotropy in the measurement direction.

In our recent work [8], we introduced a microstructural magnetic model that incorporates crystallographic textures to predict tensorial permeability anisotropy. This model represents a fundamental advance in magnetic property prediction based on crystallographic textures, relying solely on essential material properties, specifically the fundamental permeability of an elemental domain. Whilst it provides the capability to predict anhysteretic BH curves its non-linear nature results in relatively high computational demands. This aspect poses a significant challenge for applications that require extensive computations, such as inversion and optimisation problems and those involving 3D microstructures. This complexity necessitates a balance between model precision and computational efficiency, especially in scenarios where rapid or numerous calculations are essential.

In this paper, we introduce a microstructural model based on scalar permeability. The foremost attribute of this model, compared to the tensorial permeability model, is its computational speed, achieved through use of a linear-material FE model. It is worth noting this improved performance requires a more complex parameter set, specifically the single crystal permeabilities in three different directions at various magnetic fields. The challenge of determining these intricate material properties, especially in the context of commercial steels, is notable. To overcome this, a hybrid approach combining experimental techniques with modelling was taken to obtain these parameters. This integrative method enhances the model's efficiency and ensures its relevance in practical applications. Consequently, this model has become a useful tool for NDE of steel anisotropy [9]. It is especially valuable in situations where quick computation and efficient use of resources are critical, and where scalar permeability offers a reliable approximation.

2. Model

The FE microstructure model considers a magnetostatics problem that involves a uniform static field applied to the microstructure. It accepts either modelled virtual microstructures or measured electron backscatter diffraction (EBSD) data as the geometry. The model has been implemented in the AC/DC module of COMSOL Multiphysics and Livelink with MATLAB. A MATLAB-based software, EBSD Polygonizer [10], was developed to convert the raster EBSD data into polygons representing each grain ready for FE geometry. Each grain is considered as an individual entity associated with a material defining its relative permeability. A uniform background magnetic flux density, $\boldsymbol{B_b}$, is applied, together with the External Vector Potential boundary condition on the surface of a sphere or the circumference of a circle of a diameter five times larger than the microstructure dimensions representing the air in the case of the 3D or 2D model respectively, in COMSOL Multiphysics [11].

The relative permeability for grain i, μ_i, is given by an empirical relationship reported in [3], which was originally inspired by the formula of the magnetocrystalline anisotropy energy and is also analogical to the empirical relationship for the directional elastic modulus [12]:

$$\mu_i = \mu_{100} + 3(\mu_{111} - \mu_{100})(\gamma_{xi}^2\gamma_{yi}^2 + \gamma_{yi}^2\gamma_{zi}^2 + \gamma_{zi}^2\gamma_{xi}^2) \tag{1}$$

where μ_{100} and μ_{111} are the permeability of a single crystal along the $\langle 100\rangle$ and $\langle 111\rangle$ directions respectively, γ_{xi}, γ_{yi} and γ_{zi} are the direction cosine of $\boldsymbol{B_b}$ vector with respect to the [100], [010] and [001] direction respectively, which are calculated from the grain orientation data. A refined version introducing an additional single crystal permeability along the $\langle 110\rangle$ direction, μ_{110}, to improve the accuracy is given as follows after [3]:

$$\mu_i = \mu_{100} + 4(\mu_{110} - \mu_{100})(\gamma_{xi}^2\gamma_{yi}^2 + \gamma_{yi}^2\gamma_{zi}^2 + \gamma_{zi}^2\gamma_{xi}^2) + 9(3\mu_{111} + \mu_{100} - 4\mu_{110})(\gamma_{xi}^2\gamma_{yi}^2\gamma_{zi}^2) \tag{2}$$

In this paper, Eq. (2) was chosen for better fitting whilst Eq. (1) was used in Section 6. The effective permeability

$$\mu_{eff} \overset{\text{def}}{=} \frac{B}{\mu_0 H} \tag{3}$$

is averaged over the whole microstructure where μ_0 is the permeability for free space and B and H are the magnitude of the solved $\boldsymbol{B}$ and $\boldsymbol{H}$ vectors respectively. The magnitude of $\boldsymbol{B_b}$ has no influence on μ_{eff} in the model. Its direction is specified by a polar angle, θ, and an azimuthal angle, φ. In reality, it is known that permeability is dependent on the applied field and the B, which can be captured by using different μ_{100}, μ_{110} and μ_{111} for different magnitude of B.

3. Materials and experimental details

A commercial-grade GOES with a thickness of 0.27 mm and two Interstitial-Free (IF) steels – one fully recrystallised and the other partially recrystallised – were studied to validate the proposed model. The GOES, characterised as a soft magnetic material, exhibits a strong, single-component texture and high permeability. Conversely, the IF steel, a ferromagnetic structural steel, has a considerably lower permeability and a more complex, albeit weaker, texture. The two IF steel samples were taken from the same industrially processed coil, which underwent varying degrees of recrystallisation at different coil positions. As a result, they are expected to share the same μ_{100}, μ_{110} and μ_{111} parameters disregarding the effects of dislocations anticipated in the unrecrystallised regions in the partially recrystallised sample as a first approximation but differ in texture. The fully-recrystallised sample was used to identify these parameters from experimental magnetic measurements whilst the partially-recrystallised sample was employed to validate the model using the identified parameters.

For EBSD analysis, metallographic samples were prepared. EBSD data for the GOES sample covered a substantial area of approximately $12 \times 11\,\text{mm}^2$ containing 60 grains, with a step size of 10 μm, revealing very coarse grains with equivalent circular diameters (ECD) ranging from 60 μm to 10.6 mm and being 871 μm on average and a pronounced Goss ($\{110\}\langle 001\rangle$) texture, typical for this steel grade, as evidenced by the inverse pole figure (IPF) maps and the Orientation Distribution Function (ODF) map shown in Fig. 1. For the IF steel samples, EBSD data encompassed a smaller yet representative area of $398 \times 274\,\mu\text{m}^2$ containing approximately 350 grains, at a finer step size of 0.3 μm. Fig. 2 shows the IPF and the ODF maps for the IF steel samples. The fully-recrystallised sample exhibits fine equiaxed grains with an ECD of $16.8 \pm 12.0\,\mu\text{m}$ (Fig. 2(e)–(g)) and moderate $\{111\} \parallel$ ND fibre textures, Fig. 2(h). In contrast, the partially recrystallised sample displays a mix of many finer equiaxed grains and some elongated grains distributed along the RD. In addition to the $\{111\} \parallel$ ND texture, the partially-recrystallised sample also exhibits a weaker $\{110\} \parallel$ RD fibre texture, with a peak near $(0°, 27.7°, 45°)$ in the Euler space, as shown in Fig. 2(h).

Permeability measurements were conducted using an in-house 2D Rotational Single Sheet Tester (RSST). This involved measuring the permeability at various angles (φ) relative to the RD within the sheet plane (i.e., $\theta = 90°$), by rotating the $\boldsymbol{B}$ vector while maintaining its magnitude constant. These measurements were performed at 20 Hz and different magnitudes of B. Disk samples, each 80 mm in diameter, were prepared via Electron Discharge Machining for these tests. To ensure repeatability, four measurements were conducted for each sample. Between each measurement, the sample was removed, rotated by 180°, and repositioned on the apparatus. Further details about the RSST system and methodology are available elsewhere [13].

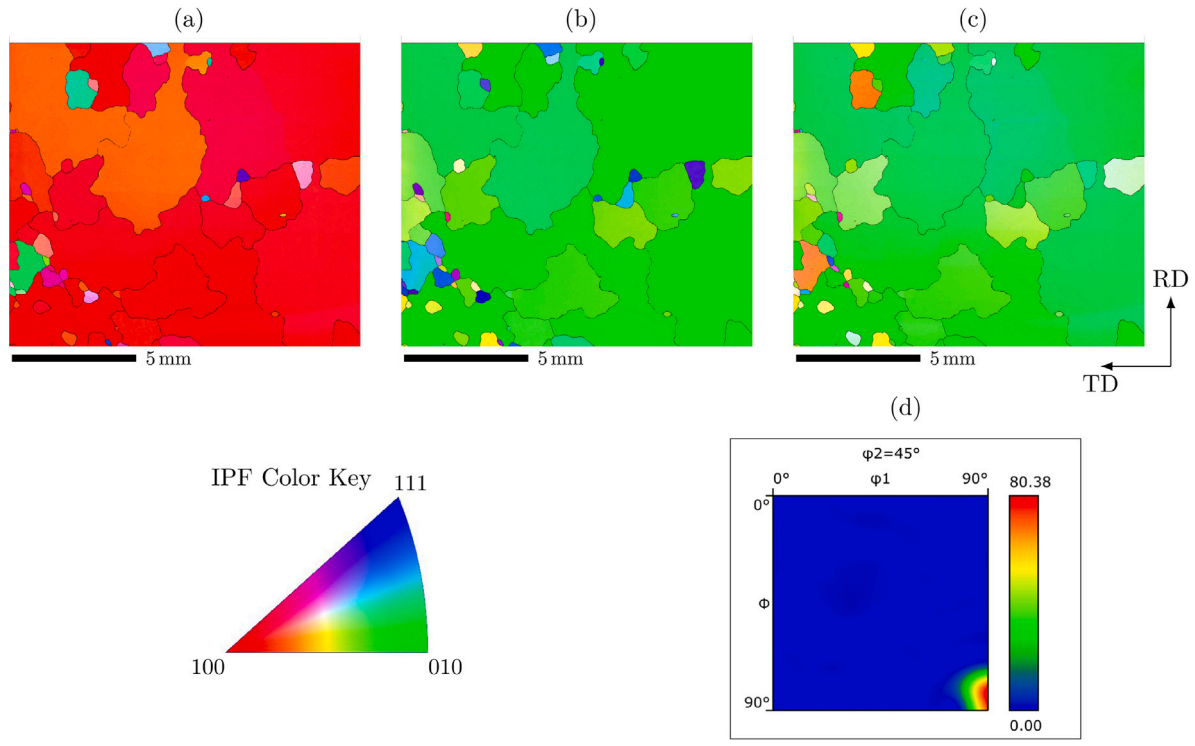

Fig. 1. IPF and ODF maps illustrating crystallographic orientations and textures of the GOES sample. Panels (a), (b), and (c) display the Rolling Direction (RD), Transverse Direction (TD), and Normal Direction (ND) poles, respectively. All IPF maps are oriented in the RD-TD plane. Panels (d) shows the ODF section for $\varphi_2 = 45°$.

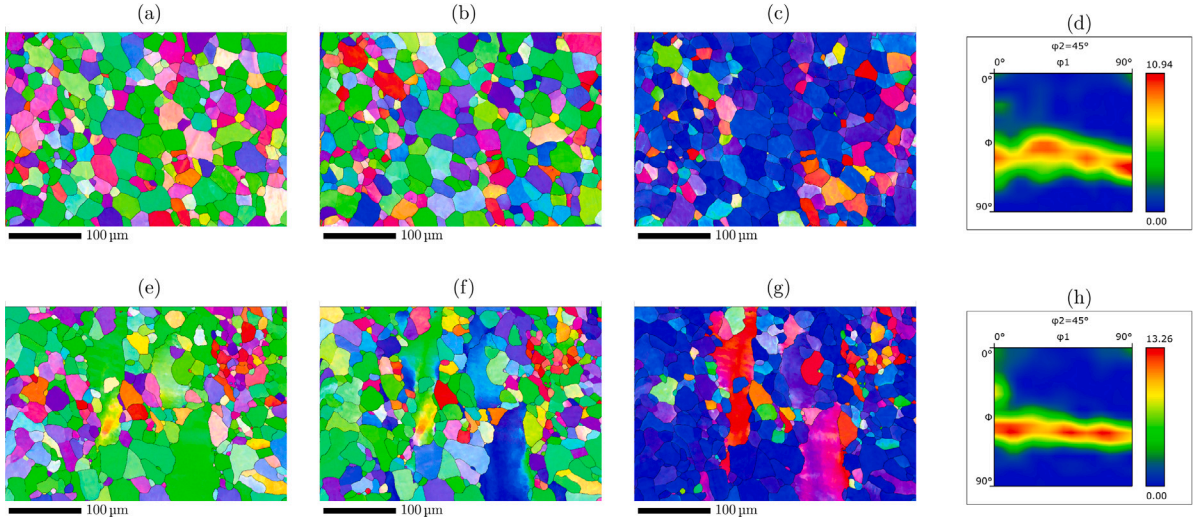

Fig. 2. IPF and ODF maps of the IF steel samples illustrating their crystallographic orientations and textures. Panels (a), (b) and (c) display the RD, TD and ND poles of the IPF maps respectively and panel (d) the ODF map for the $\varphi_2 = 45°$ section, for the fully-recrystallised sample. Panels (e), (f), (g) and (h) display the counterparts for the partially-recrystallised one.

4. Identification of the model parameters

Fig. 3 showcases a comparison between the measured and predicted anisotropic permeability curves at various angles relative to the RD under different magnetic field strengths (B). Model parameters were identified through optimisation, specifically, non-linear least square fitting the predicted permeability values with the measurements. The optimisation procedure is described in detail in Appendix. The identified single crystal permeability parameters are detailed in Table 1.

Overall, the predictions align reasonably well with the experimental data, particularly at higher B values, such as 1.3 T for the GOES sample, where crystallographic texture plays a more significant role. Notably, at lower fields (Fig. 3(a)–(c)), the GOES sample exhibits an anisotropy unexpected of purely crystallographic texture effects, with permeability around 55° from the RD (close to ⟨111⟩ directions) being higher than along the TD (near ⟨110⟩ directions). This discrepancy may be attributed to stress effects from the coating, enhancing GOES performance along the RD but significantly reducing permeability along the TD [14]. Consequently, the fitted $\mu_{110} < \mu_{111}$. At higher B, the influence of crystal orientation becomes more pronounced, overshadowing the stress effects.

For the fully-recrystallised IF steel samples, the fit with experimental data is relatively accurate. The fitted parameters indicate μ_{111} =

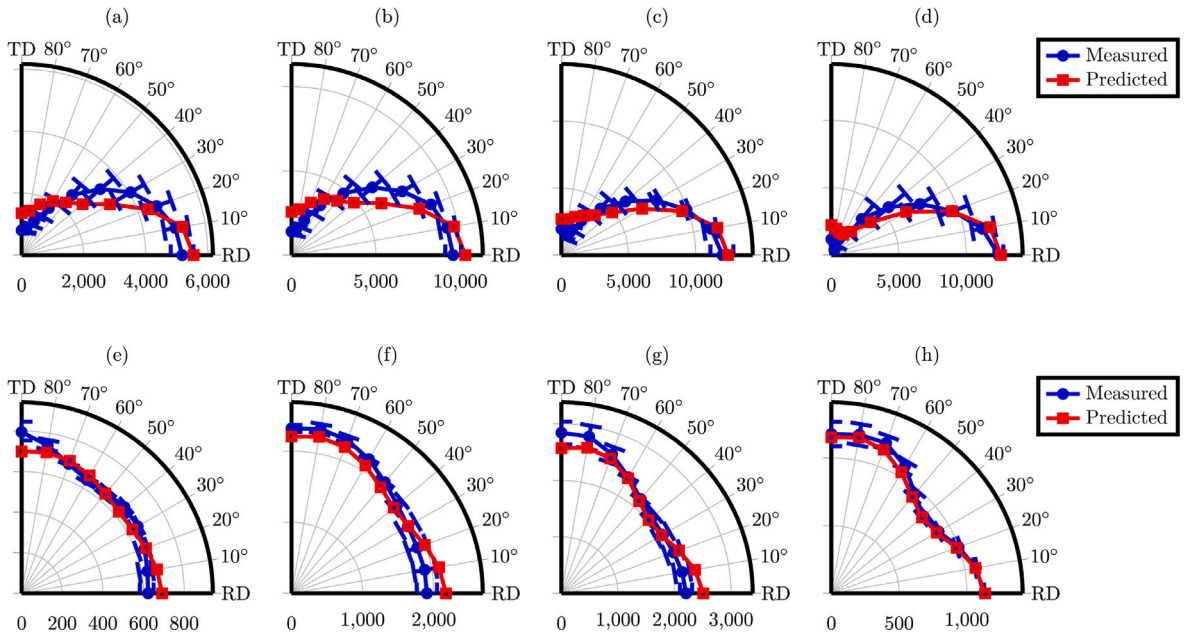

Fig. 3. Predicted permeability curves at various angles relative to RD with different model parameters, i.e., the single crystal permeability values corresponding for different magnetic fields (B) for GOES and the fully-recrystallised IF Steel Samples, alongside experimental measurements. The error bars represent the standard deviation of the measured permeability data. Panels (a) to (d) illustrate the permeability curves for the GOES sample at magnetic field strengths (B) of 0.1 T, 0.5 T, 0.9 T, and 1.3 T, respectively. Panels (e) to (h) display corresponding curves for the fully recrystallised IF steel sample.

Table 1
Identified model parameter values for the single-crystal permeability along the ⟨111⟩, ⟨110⟩ and ⟨100⟩ directions.

Materials	B (T)	μ_{111}	μ_{110}	μ_{100}
GOES	0.1	2395	1	7398
	0.5	4594	29	13 736
	0.9	3505	1.2	16 716
	1.3	717	24	17 122
IF Steel	0.1	466	466	1532
	0.5	1163	1163	5950
	0.9	825	825	8824
	1.3	292	292	4347

μ_{110}, leading to a simplification of Eq. (2) to Eq. (1), discounting the higher order term of $\gamma_{xi}^2\gamma_{yi}^2\gamma_{zi}^2$. In this scenario, only two parameters, μ_{111} and μ_{100}, are required to achieve similar accuracy.

Fig. 4(a) to (c) presents the predicted permeability maps using the fitted parameters for $B = 1.3$ T for the RD, TD, and ND of the GOES sample, respectively. The RD map predominantly displays high permeability values, indicated by more red hues, aligning with the IPF maps despite a visually distinct colour resolution due to different colour spaces representing varied data types. Conversely, the TD and ND maps predominantly show lower permeability, evidenced by bluer tones.

Similarly, Fig. 4(d) to (f) illustrate the predicted permeability maps for $B = 1.3$ T for the RD, TD, and ND of the full-recrystallised IF steel sample. Here, a consistent correlation with the IPF maps is observed. The ND map, in particular, displays predominantly low permeability values, indicated by a darker and more uniform blue, correlating with the {111} ∥ ND texture observed in the IPF maps (Fig. 2(c)). The RD and TD maps, on the other hand, show higher and more randomly distributed permeability values, further substantiating this consistency.

In this study, while the primary focus is on magnetic anisotropy within the sheet plane (i.e., $\theta = 90°$), it is important to note that the model's applicability is not confined to specific directions or crystal orientations. This versatility enables the prediction of magnetic anisotropy for a broad spectrum of directions and crystallographic textures, even those not readily accessible through experimental measurements. The strength of this model also lies in its microstructural approach, which integrates crystallographic texture analysis. Consequently, magnetic permeability values and other magnetic parameters can be mapped onto individual grains, analogous to how crystallographic orientations are assigned in an IPF map relative to a specimen coordinate system.

This capability allows the permeability map to serve as a complementary visual representation of crystal orientations. It also provides a qualitative measure of texture quality. These attributes render the proposed FE microstructure model a useful tool for the quantitative prediction of magnetic anisotropy in ferritic steels and for tailoring microstructure and crystallographic texture to achieve desired magnetic properties.

To validate the model, the parameters identified for the IF steel using the fully-recrystallised sample were employed to predict the permeability curves for the partially-recrystallised sample. Fig. 5 demonstrates that the predictions generally align well with the experimental measurements. It is important to note that the model does not account for the effects of dislocations expected within the non-recrystallised, elongated grains in the partially-recrystallised sample. These dislocations predominantly form sub-grain boundaries. Although this could be considered as a grain size effect and thus incorporated into the model, doing so would significantly increase the computational cost associated with microstructure data processing and subsequent FE modelling. Moreover, we lack a suitable set of samples with constant or random textures and varying grain sizes needed to derive the corresponding model parameters for grain size. The consideration of grain size based on virtual microstructures and random textures is discussed in Section 6.

5. Comparison with the tensor permeability model

Fig. 6 presents the predicted permeability anisotropy for typical crystallographic textures, compared with results from the tensorial permeability model reported in [8]. This comparison demonstrates that the scalar permeability model closely mirrors the anisotropy behaviours predicted by the tensorial model. These behaviours align with expectations for these textures. Notably, all curves are symmetric around the 90° axis, reflecting the cubic crystal and specimen symmetry. The highest permeability values are observed at the RD for the η fibre

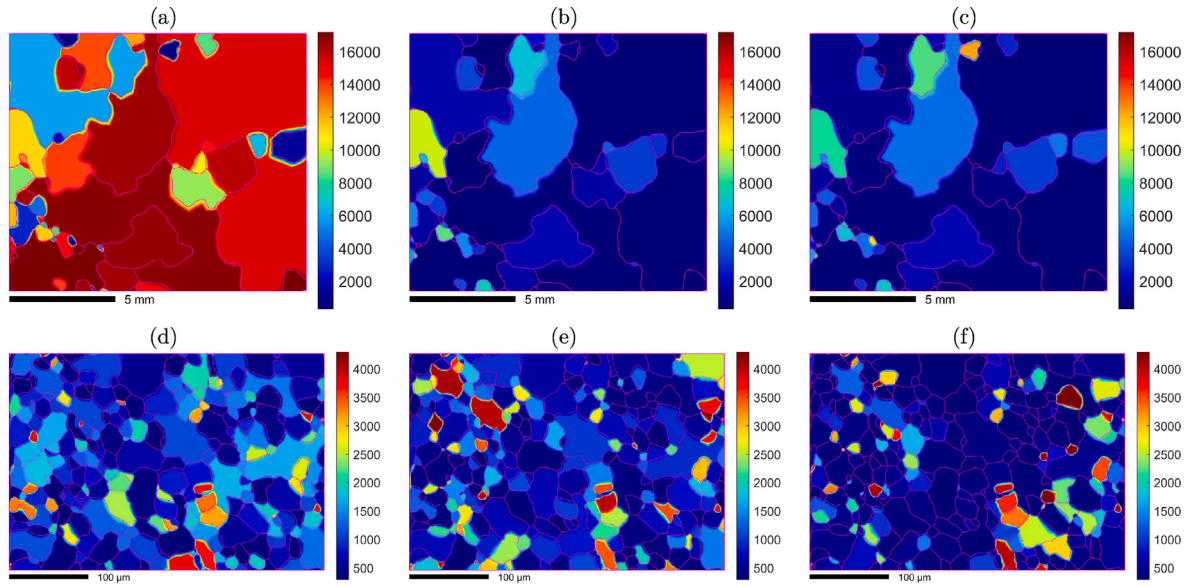

Fig. 4. Predicted permeability maps for different field directions. Panels (a) to (c) illustrate the permeability when the applied field is aligned with the RD, TD and ND for the GOES sample, respectively. Panels (d) to (f) depict similar orientations (RD, TD, and ND) for the full-recrystallised IF steel sample.

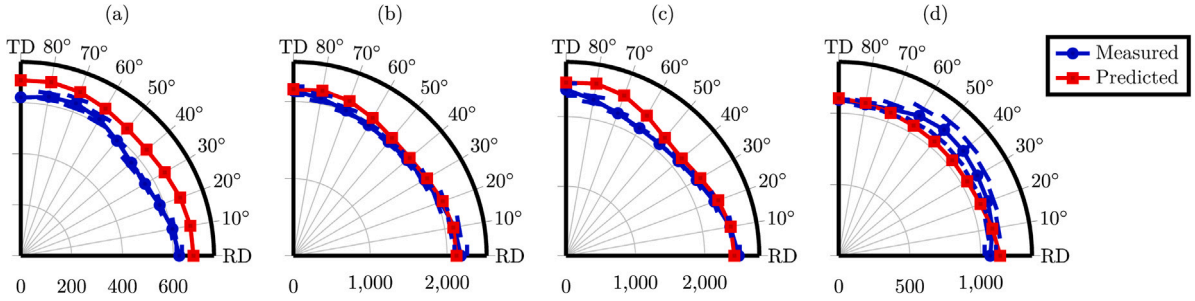

Fig. 5. Predicted permeability curves for the partially recrystallised IF steel sample at various angles relative to RD using the identified IF model parameters given in Table 1. The error bars represent the standard deviation of the measured permeability data. Panels (a) to (d) correspond to different magnetic field strengths (B) at 0.1 T, 0.5 T, 0.9 T, and 1.3 T, respectively.

and Goss texture, both representing ⟨100⟩ directions, the magnetic easy direction. Conversely, the lowest values occur around 54.7° from the RD for the Goss texture, aligning with the ⟨111⟩ direction, known as the magnetic hard direction. Both the γ fibre and the θ fibre display isotropic permeability within the microstructure plane, consistent with their in-plane random orientations as a ND fibre, leading to an averaging out effect. Specific parameters, including $\mu_{100} = 413$, $\mu_{110} = 355$, and $\mu_{111} = 333$ were obtained by fitting with the tensor permeability model prediction for the Goss texture only and then employed directly in modelling other textures.

The scalar permeability model exhibits notable computational efficiency, operating one to two orders of magnitude faster than the tensor permeability model. For the identical 2D microstructure and meshing as an example, the scalar model requires approximately 35 s on average to predict a data point on the curve, in contrast to the tensor model, which takes 1250 s using the same computing setup.

6. Consideration of grain size

Incorporating grain size effects into permeability modelling requires adjusting each grain's permeability, μ_i, based on its size, d. Presently, there is no consensus on an empirical relationship between grain size and permeability, but two predominant theories are often referenced: the $1/d$ relationship (Landgraf et al. [15]) and the $1/\sqrt{d}$ relationship (Goodenough [16]). Our previous tensorial permeability model [8] utilised the former, correlating permeability changes with the reduction of elementary domains at grain boundaries. Alternatively, the latter theory draws parallels with the Hall-Petch relationship, treating grain boundaries as domain pinning sites, akin to barriers in dislocation movement.

In this work, we adopt a generalised power law approach to model this relationship:

$$\mu_{gi} = \mu_i - \frac{c_g}{d_i^n} \tag{4}$$

Here, d_i is the ECD of grain i, c_g is a constant independent of grain size, and n can be 0.5, 1, or another positive number determined experimentally. The value μ_i represents the permeability limit as $d_i \to +\infty$, effectively the relative permeability of a single crystal with the same orientation as grain i.

Fig. 7(a) depicts a series of 3D microstructures within a 0.25 mm × 0.25 mm × 0.25 mm cube, each comprising a different number of grains, thus varying the average grain size. These microstructures, with random crystallographic orientations, were generated using Laguerre tessellation in Neper [17]. A broader range of grain sizes was obtained by adjusting the cube size while maintaining a constant grain count of 400, thus expanding the grain size spectrum without exceeding computational limits. The tessellation's seed attributes were optimised to achieve a lognormal grain size distribution, similar to that observed in uniform equiaxed steels (Fig. 7(b)).

Fig. 7(c) illustrates that the predicted μ_{eff}^g, effective permeability for a whole microstructure, increases with average grain size, adhering to the power law described in Eq. (4). Different values of c_g and n were

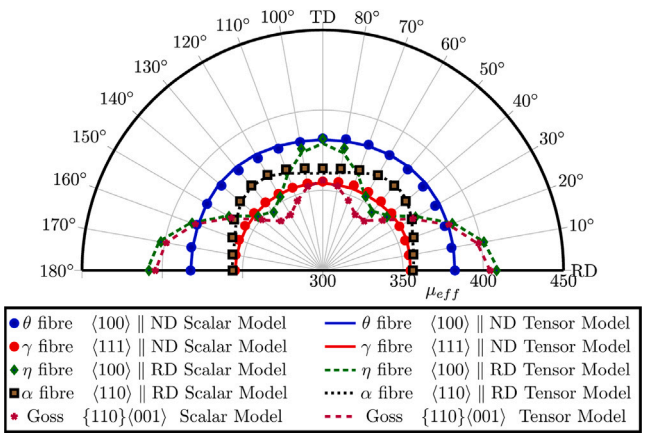

Fig. 6. The predicted effective permeability for some typical textures using the present scalar permeability model and the tensorial permeability model.

applied in this analysis. Specifically, the $1/\sqrt{d}$ rule (i.e., $n = 0.5$) aligns well with experimental measurements reported in [18]. The model parameters, including $c_g = 25\,\mu m^{0.5}$, $\mu_{100} = 601$, and $\mu_{111} = 379$, were optimised via least square fitting with these measurements. The fitted pre-exponent constant (454) is close to the μ_{eff} values for $c_g = 0$, affirming the model's capability in representing grain size effects.

The experimental data reported in [18] span a limited grain size range, approximately 3 μm to 65 μm, fitting well with the equation $y = 489 - 564.3/x^{0.33}$. Predictions for $n = 1$ also show good agreement with the $1/d$ rule, specifically $y = 460 - 2365/x$, for grain sizes above 8 μm. The discrepancy observed at smaller grain sizes can be attributed to the chosen c_g, which leads to setting μ_{gi} for numerous grains to 1 if Eq. (4) results in $\mu_{gi} < 1$.

Interestingly, the FE model's interaction with magnetic flux in grains of various sizes and shapes does not inherently capture the grain size effect. This is evident from the insensitivity of μ_{eff} values to grain size for $c_g = 0$, as shown in Fig. 7(c). This phenomenon is primarily attributed to the magnetic domain structure's influence on initial permeability, a factor not easily incorporated into the classical electromagnetic framework of this model. Our proposed empirical power law relationship serves as a practical initial approximation for modelling grain size effects.

Furthermore, the model adeptly averages the anisotropy of individual grains. This is demonstrated by the reducing variability of μ^g_{eff} with an increasing number of grains in Fig. 7(c), mirroring similar behaviours observed in FE modelling of elastic modulus in polycrystalline materials [19].

7. Conclusions

In conclusion, the developed scalar permeability finite element microstructure model, which integrates crystallographic texture, has demonstrated its proficiency in accurately predicting anisotropic magnetic permeability for specific microstructures. This model has undergone preliminary validation with a commercial Grain-Oriented Electrical Steel (GOES) characterised by coarse grains and a strong Goss texture; and further experimental validation with another distinct type of steels, two industrially recrystallised Interstitial-Free (IF) steel, notable for its finer grains and a more complex yet weaker texture.

A key finding of this study is that the scalar model's predictions of anisotropic effective permeability not only align closely with those from the tensor permeability model for typical textures but also offer a significant increase in computational efficiency. In fact, the scalar model operates one to two orders of magnitude faster than its tensor counterpart, making it particularly advantageous in scenarios demanding rapid computation and efficient resource management.

Furthermore, the model's ability to encapsulate the grain size effect via a generalised power law is corroborated by experimental data from the literature. Additionally, its capacity to represent averaging effects is evidenced by applying it to microstructures with varying grain counts. This capability underscores the model's utility in accurately simulating the impact of microstructural variations on magnetic properties.

Overall, the scalar permeability finite element microstructure model proves to be a valuable tool in magnetic materials research and applications, especially when scalar permeability provides a suitable approximation and when time and computational resources are of the essence.

CRediT authorship contribution statement

Jun Liu: Writing – review & editing, Writing – original draft, Visualization, Validation, Software, Methodology, Investigation, Data curation, Conceptualization. **Claire Davis:** Writing – review & editing, Supervision, Resources, Funding acquisition. **Shuaichao Yue:** Validation, Methodology. **Mohsen Aghadavoudi Jolfaei:** Validation. **Jialong Shen:** Methodology, Investigation. **Yongjian Li:** Supervision.

Declaration of competing interest

The authors declare that they have no known competing financial interests or personal relationships that could have appeared to influence the work reported in this paper.

Acknowledgements

Prof Claire Davis and Dr Jun Liu acknowledge support from the Engineering and Physical Sciences Research Council (EPSRC), United Kingdom under Grant EP/P027210/1. Prof Yongjian Li and Dr Shuaichao Yue acknowledge support from the National Natural Science Foundation of China (NSFC) under Grant 52130710. Dr Jialong Shen acknowledges support from NSFC under Grant 52464039. We extend our gratitude to Ms Yating Li and Dr Chris Harrison of Cardiff University for their invaluable assistance with the magnetic measurements.

Appendix

The optimisation process for determining the single crystal permeabilities, μ_{111}, μ_{110} and μ_{100}, along the crystallographic directions ⟨111⟩, ⟨110⟩ and ⟨100⟩ respectively, is detailed below and illustrated in the flow chart in Fig. A.1.

1. Make an educated guess of μ_{100}, μ_{110} and μ_{111}, collectively referred to as a variable vector $\boldsymbol{X}$, based on previous literature.
2. Solve the scalar permeability finite element model using $\boldsymbol{X}$ and calculate the effective permeability values, μ_{eff}, for series of directions, referred to as a vector $\boldsymbol{\mu}_{predicted}$.
3. Compare $\boldsymbol{\mu}_{predicted}$ with the measured permeability values in the above directions, $\boldsymbol{\mu}_{measured}$.
4. If the difference between $\boldsymbol{\mu}_{predicted}$ and $\boldsymbol{\mu}_{measured}$ exceeds a tolerance ξ, $\boldsymbol{X}$ is adjusted iteratively according to the Nonlinear Least Squares algorithm in MATLAB. The process repeats until the difference falls below ξ, at which point the final $\boldsymbol{X}$ values are output as the fitted single crystal permeabilities.

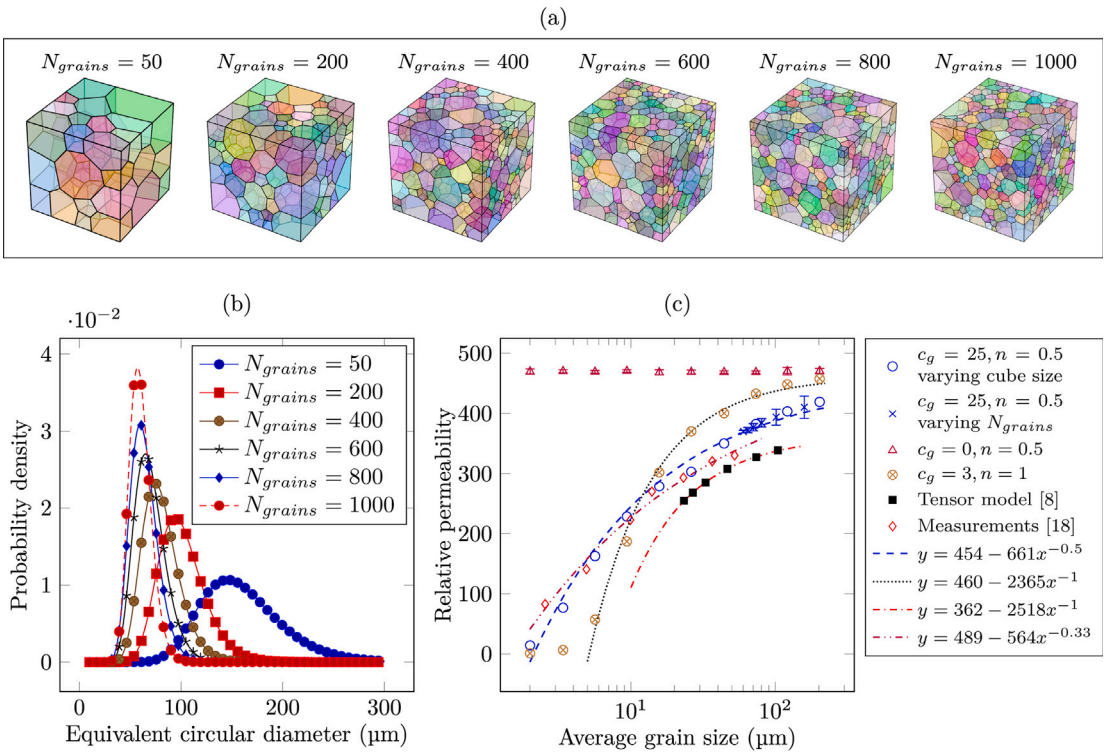

Fig. 7. Illustration of 3D microstructures and permeability analysis. Panel (a) displays a series of 3D microstructures with varying grain sizes. Panel (b) shows the grain size distribution. Panel (c) presents the predicted effective permeability as a function of average grain size (measured by equivalent circular diameter) using different parameters for the power law relationship. These predictions are compared against the baseline scenario where the grain size effect is not considered ($c_g = 0$), as well as against the measured relative permeability for low carbon steels as reported in [18] and predictions from the tensorial permeability model [8]. The lines in the graph indicate a strong correlation with the power law relationship.

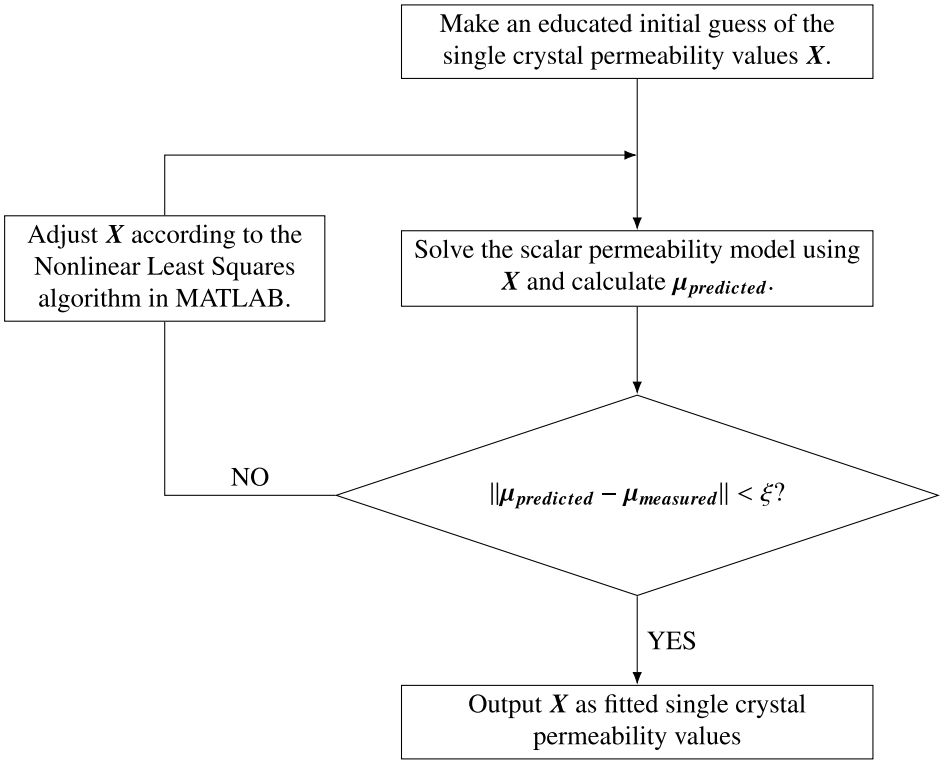

Fig. A.1. Flow chart for the optimisation process for determining the single crystal permeability values.

References

[1] X. Hao, W. Yin, M. Strangwood, A. Peyton, P. Morris, C. Davis, Modelling the electromagnetic response of two-phase steel microstructures, NDT E Int. 43 (4) (2010) 305–315, http://dx.doi.org/10.1016/j.ndteint.2010.01.006.

[2] R.E. Newnham, Magnetic phenomena, in: Properties of Materials : Anisotropy, Symmetry, Structure, Oxford University Press, 2005, pp. 122–146.

[3] L. Daniel, R. Corcolle, A note on the effective magnetic permeability of polycrystals, IEEE Trans. Magn. 43 (7) (2007) 3153–3158, http://dx.doi.org/10.1109/TMAG.2007.896228.

[4] L. Kestens, S. Jacobs, Texture control during the manufacturing of nonoriented electrical steels, Texture Stress. Microstruct. 2008 (2008) 1–9, http://dx.doi.org/10.1155/2008/173083.

[5] A. Bükki-Deme, I. Szabó, C. Cserháti, Effect of anisotropic microstructure on magnetic barkhausen noise in cold rolled low carbon steel, J. Magn. Magn. Mater. 322 (13) (2010) 1748–1751, http://dx.doi.org/10.1016/j.jmmm.2009.12.020.

[6] L. Zhou, C. Davis, P. Kok, F. Van Den Berg, S. Labbé, A. Martinez-de Guerenu, D. Jorge-Badiola, I. Gutierrez, Magnetic {ndt} for steel microstructure characterisation – modelling the effect of ferrite grain size on magnetic properties, in: 19th World Conf. Non-Destructive Test. (WCNDT 2016), Vol. 21, No. 7, NDT.net, Munich, Germany, 2016.

[7] L. Zhou, J. Shen, A. Martinez-De-Guerenu, D. Jorge-Badiola, I. Gutiérrez, P. Kok, F. van den Berg, S. Labbé, A. Skarlatos, C. Reboud, P. Lombard, Micro and macro microstructure modelling for the influence of grain size on magnetic properties in structural steel and modelled commercial sensor outputs, in: 12th ECNDT, Gothenberg, 2018, pp. ECNDT–0228–2018.

[8] J. Liu, C. Davis, Tensorial permeability microstructure model considering crystallographic texture and grain size for evaluation of magnetic anisotropy in polycrystalline steels, Phil. Mag. 101 (10) (2021) 1224–1244, http://dx.doi.org/10.1080/14786435.2021.1892229.

[9] M. Aghadavoudi Jolfaei, J. Liu, L.F. Zhou, F. Van Den Berg, C. Davis, Non-destructive evaluation of magnetic anisotropy associated with crystallographic texture of interstitial free steels, J. Magn. Magn. Mater. 568 (October 2022) (2023) 170374, http://dx.doi.org/10.1016/j.jmmm.2023.170374.

[10] J. Liu, EBSDPolygonizer: Enabling realistic microstructural modelling, SoftwareX 25 (2024) 101622, http://dx.doi.org/10.1016/j.softx.2023.101622.

[11] COMSOL, AC/DC Module User's Guide, in: AC/DC Module User's Guide, 6.0, COMSOL, 2021.

[12] R.K. Ray, J.J. Jonas, M.P. Butrón-Guillén, J. Savoie, Transformation textures in steels, ISIJ Int. 34 (12) (1994) 927–942, http://dx.doi.org/10.2355/isijinternational.34.927.

[13] S. Yue, A.J. Moses, P.I. Anderson, C. Harrison, Y. Li, Q. Yang, Measurement and analysis of the non-symmetry of transverse magnetisation and resulting loss in grain-oriented steel using a modified RSST, J. Magn. Magn. Mater. 561 (2022) 169671, http://dx.doi.org/10.1016/j.jmmm.2022.169671.

[14] S. Washko, E. Choby, Evidence for the effectiveness of stress coatings in improving the magnetic properties of high permeability 3% Si-Fe, IEEE T. Mag. 15 (6) (1979) 1586–1591, http://dx.doi.org/10.1109/TMAG.1979.1060469.

[15] F.J.G. Landgraf, J.R.F. da Silveira, D. Rodrigues-Jr., Determining the effect of grain size and maximum induction upon coercive field of electrical steels, J. Magn. Magn. Mater. 323 (18–19) (2011) 2335–2339, http://dx.doi.org/10.1016/j.jmmm.2011.03.034.

[16] J.B. Goodenough, A theory of domain creation and coercive force in polycrystalline ferromagnetics, Phys. Rev. 95 (4) (1954) 917–932, http://dx.doi.org/10.1103/PhysRev.95.917.

[17] R. Quey, M. Kasemer, The neper/FEPX project: Free / open-source polycrystal generation, deformation simulation, and post-processing, IOP Conf. Ser.- Mat. Sci. 1249 (1) (2022) 012021, http://dx.doi.org/10.1088/1757-899x/1249/1/012021.

[18] L. Zhou, C. Davis, P. Kok, Steel microstructure – magnetic permeability modelling: The effect of ferrite grain size and phase fraction, J. Magn. Magn. Mater. 519 (2021) 167439, http://dx.doi.org/10.1016/j.jmmm.2020.167439.

[19] M. Kamaya, A procedure for estimating Young's modulus of textured polycrystalline materials, Int. J. Solids Struct. 46 (13) (2009) 2642–2649, http://dx.doi.org/10.1016/j.ijsolstr.2009.02.013.